Energy-based evaluation of liquefaction potential under non-uniform cyclic loading

Ricardo J.N. Azeiteiro[a,*], Paulo A.L.F. Coelho[b], David M.G. Taborda[c] and José C.D. Grazina[d]

[a] PhD candidate, Department of Civil Engineering, University of Coimbra

Rua Luís Reis Santos- Pólo II da Universidade, 3030-788 Coimbra, Portugal

ricardoazeiteiro@uc.pt

[*] corresponding author (Tel: +351239797265; Fax: +351 239 797 267)

[b] Assistant Professor, Department of Civil Engineering, University of Coimbra

Rua Luís Reis Santos- Pólo II da Universidade, 3030-788 Coimbra, Portugal

pac@dec.uc.pt

[c] Lecturer, Department of Civil and Environmental Engineering, Imperial College London

Skempton Building, South Kensington Campus, London SW7 2AZ

d.taborda@imperial.ac.uk

[d] Assistant Professor, Department of Civil Engineering, University of Coimbra

Rua Luís Reis Santos- Pólo II da Universidade, 3030-788 Coimbra, Portugal

graza@dec.uc.pt

Soil Dynamics and Earthquake Engineering – Accepted for publication 2nd November 2016

Energy-based evaluation of liquefaction potential under non-uniform cyclic loading

Ricardo J.N. Azeiteiro, Paulo A.L.F. Coelho, David M.G. Taborda and José C.D. Grazina

Abstract

Uniform cyclic loading is commonly used in laboratory tests to evaluate soil resistance to earthquake-induced liquefaction, even if the cyclic stresses induced by earthquakes in the field are highly irregular. This paper discusses the use of stress and energy-based approaches to evaluate the liquefaction resistance of sand under irregular loading. Results of undrained cyclic triaxial tests including a large-amplitude singular peak loading cycle are presented and compared to those obtained using uniform loading. Although samples are subjected to loading patterns which would have been deemed equivalent by conventional stress-based methods, the number of cycles required to trigger liquefaction strongly depends on the amplitude and location of the peak within the loading history. Conversely, a unique relationship exists between the accumulation of dissipated energy per unit volume, computed using stress and strain measurements, and the observed residual pore water pressure build-up for all tests, throughout the entire cyclic loading application. This demonstrates that conventional laboratory tests using uniform loading conditions can be employed to determine liquefaction resistance if their interpretation is carried out based on energy principles.

Keywords: liquefaction potential; undrained cyclic triaxial tests; non-uniform cyclic loading; stress-path dependency; energy-based approach.

1. Introduction

Earthquake-induced soil liquefaction has been a subject of intensive research during the last decades. This phenomenon involves significant loss of the soil's strength and stiffness due to excess pore water pressure build-up, as well as a concurrent dissipation of energy mainly by frictional mechanisms (Okada and Nemat-Nasser 1994). Based on the assumption made by Nemat-Nasser and Shokooh (1979) that pore water pressure generation can be uniquely related to the cumulative energy dissipated per unit volume of soil up to the onset of liquefaction, several energy-based procedures for the evaluation of liquefaction potential of sand have been developed (e.g. Davis and Berrill 1982; Berrill and Davis 1985; Law *et al.* 1990; Figueroa *et al.* 1994; Dief and Figueroa 2007; Kokusho 2013). According to Liang *et al.* (1995), when compared to alternative stress-based (e.g. Seed and Idriss 1971; Seed *et al.* 1975; Idriss and Boulanger 2006) and strain-based (e.g. Dobry *et al.* 1982) approaches, energy-based methods have the strong advantage of accounting for both induced shear stress and strain, thus avoiding the need to decompose the irregular shear stress (or strain) time histories to find an equivalent uniform loading.

In order to verify the suitability of the energy concept for liquefaction evaluation, several laboratory testing programmes were designed to verify the uniqueness of the relationship between pore water pressure build-up and dissipated energy per unit volume. In particular, a series of undrained cyclic triaxial tests in which the energy content of the specimens was continuously monitored were performed by Simcock *et al.* (1983). A greater energy dissipation was observed as excess pore water pressure increased. Further evidence on the satisfactory relationship between these quantities was presented by Towhata and Ishihara (1985). Indeed, based on results of torsional shear tests using different loading patterns, the authors concluded that the relationship between excess pore water pressure generation and dissipated energy per unit volume is unique throughout the entire test, being independent of the shear stress path

followed in each test. A similar conclusion was drawn by Baziar and Sharafi (2011) and Kokusho (2013) when analysing results of undrained hollow cylinder torsional tests and undrained cyclic triaxial tests, respectively.

The laboratory testing programme performed by Figueroa and his co-workers (Figueroa *et al.* 1994; Liang *et al.* 1995; Dief and Figueroa 2007) is also noteworthy. These authors concluded that the energy required for the onset of liquefaction – known as capacity energy – was practically independent of the loading pattern used (uniform and non-uniform) and type of test performed (torsional cyclic shearing and centrifuge experiments). These results seem to be confirmed by the recent study of Polito *et al.* (2013), where cyclic triaxial tests using three different uniform loading shapes (sinusoidal, triangular and rectangular), as well as two irregular patterns where performed.

In this paper, a laboratory testing programme was carried out using a non-uniform loading pattern absent from previous research, characterising shock-type earthquakes – i.e. ground motions where the maximum induced shear stress is clearly higher than the remaining shear stress history (Ishihara and Yasuda 1975). This experimental programme aimed at comprehensively investigating the applicability of stress- and energy-based approaches to the prediction of the effect of a singular large-amplitude peak load on the liquefaction resistance of sand. Indeed, the study of a large number of earthquake records has shown that the location and magnitude of the peak acceleration varies widely between seismic events. As a result, in this paper, undrained cyclic triaxial tests in which a singular peak loading cycle of larger amplitude was applied within an otherwise uniform loading pattern were performed. Both the location and magnitude of the peak loading cycle were systematically varied in each test, highlighting the influence of an earlier or later crossing of the phase transformation line (Ishihara et al. 1975) on the liquefaction resistance of sand. Moreover, conventional undrained cyclic triaxial tests using uniform loading were also carried out in order to assess whether

stress-based methods can adequately deal with the irregularity of loading. The stress oscillations imposed in these conventional tests were chosen to be equivalent to those imposed in the non-uniform triaxial tests in accordance with the methodology proposed by Seed and Idriss (1971) and Idriss and Boulanger (2006). Based on the obtained results, it is discussed whether or not conventional laboratory tests using uniform loading can be reliably used for the evaluation of liquefaction resistance. The complete set of experimental results are subsequently interpreted using an energy-based approach. The relationships between the excess pore water pressure generation, the observed double amplitude axial strain and the accumulation of dissipated energy per unit volume are examined throughout the entire test. Conclusions are drawn about the ability of energy-based methods to accommodate the loading irregularity observed in real earthquake motions.

2. Laboratory testing programme

2.1. Material and equipment used

All tests in this experimental programme were performed on reconstituted samples of Coimbra sand, which characterises the deposits located along the banks of the Mondego River, Portugal. Analyses of the major seismic events occurred in Portugal show that these deposits are susceptible to liquefaction (Jorge and Vieira 1997).

Coimbra sand is a fine-grained sand, with sub-rounded to sub-angular particles. In order to avoid segregation, only the fraction between the no. 40 (0.425 mm) and no. 100 (0.150 mm) sieves of the ASTM series was used, resulting in a uniformly graded material. The mean particle diameter, D_{50}, and the uniformity coefficient, C_u, are approximately 0.28 mm and 1.6, respectively. The density of soil particles, G_s, is 2.65 and the minimum and maximum void ratios, e_{min} and e_{max}, determined according to ASTM D4253-00 (2006) and ASTM D4254-00 (2006), are close to 0.48 and 0.81, respectively. The behaviour of this sand has been extensively

studied within the small to large strain range and under different type of solicitations as part of a collaborative research project (e.g. Santos *et al.* 2012).

A fully computer-controlled hydraulic triaxial apparatus of the Bishop and Wesley (1975) type, designed for 38 mm diameter specimens, was used to perform the cyclic triaxial tests. In order to apply extension loading, a flexible sleeve connecting a top cap to a reaction head was used.

2.2. Experimental procedures

Air-pluviation of dry sand was used to prepare samples with a height/diameter ratio close to 2 and a void ratio of about 0.67, i.e. with a relative density close to 40 %. The desired density was controlled by the rate of pouring, which depended on the size and number of openings of a miniature container. The height of pouring, which also affects the resulting relative density, was kept approximately constant during sample preparation by raising the container while pouring the sand, ensuring the uniformity of the specimens in height. The pouring technique was methodically tested to guarantee accuracy and repeatability, with the density of the produced samples being confirmed from mass and volume measurements after preparation. A small suction of about 5 kPa was used to sustain the sample after dismounting the mould used during sand pouring.

All samples were saturated by flowing de-aired water through the sample, always at very low effective confining stresses, until a Skempton's B-value above 0.98 was measured in all tests. Subsequently, samples were isotropically consolidated to an effective pressure of 100 kPa. A back-pressure of 400 kPa, used during the saturation stage, was kept during this consolidation stage, to ensure that the sample remained saturated. Undrained cyclic shear loading was applied afterwards, until large strains and excess pore water pressures were measured.

2.3. Location and magnitude of the singular peak

Undrained cyclic triaxial (UCT) tests having a singular peak loading cycle of much larger amplitude than the remaining constant amplitude loading were conducted on samples of

Coimbra sand to study the effect of the largest earthquake-induced stress cycle on the liquefaction resistance of sand. In order to define realistic amplitudes and locations of the peak loading cycle to be used in the laboratory tests, real earthquake records were analysed. Specifically, bedrock horizontal acceleration time series of 132 earthquakes, which occurred around the world, ranging from the 1935 Helena earthquake to the 2015 Nepal earthquake, were collected (Appendix). For each horizontal motion, the maximum and average accelerations, a_{max} and a_{av}, respectively, the cycle at which the maximum acceleration was registered, $N(a_{max})$, and the total number of loading cycles, N_{tot}, were assessed. While a_{max} was directly obtained from each accelerogram data, representative values of each ground motion were selected to determine a_{av}, $N(a_{max})$ and N_{tot}. In particular, a low-amplitude cut-off level was used to prevent many cycles of small amplitude from inappropriately influencing the obtained results (Hancock and Boomer 2005). According to Seed *et al.* (1995), loading cycles having amplitudes less than about 30 % of the maximum amplitude do not have a significant contribution to the onset of liquefaction and, therefore, a cut-off level of 0.30 a_{max} was adopted in the present study. All peak accelerations having an amplitude greater than 0.30 a_{max} were then selected and used to estimate a_{av}, $N(a_{max})$ and N_{tot}. Fig. 1 illustrates the application of this methodology to the 1989 Loma Prieta earthquake.

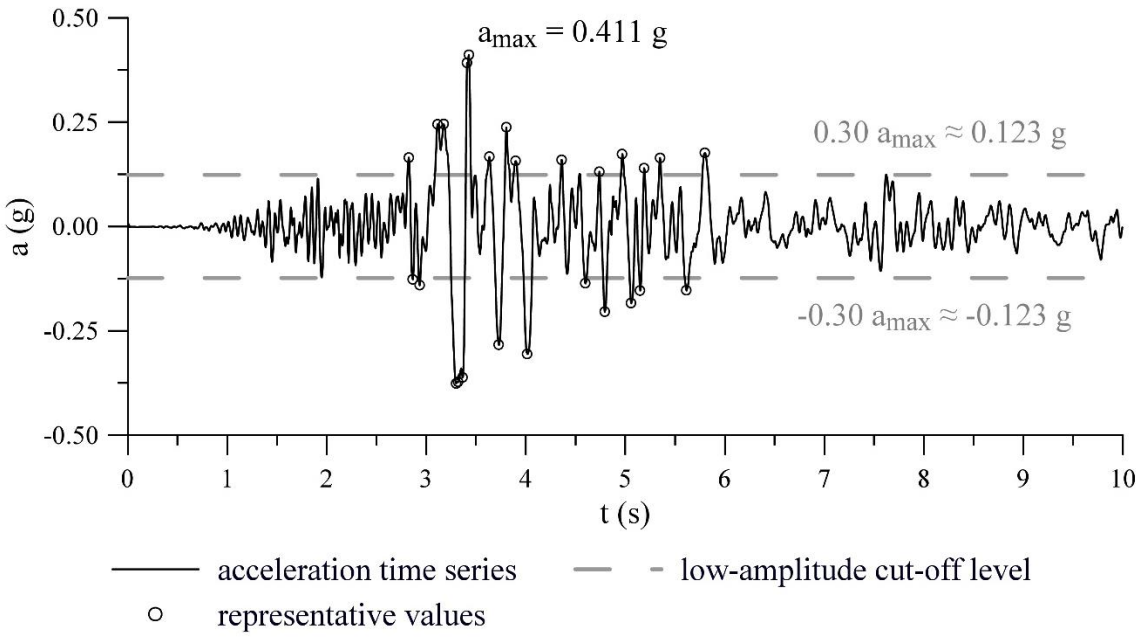

Fig. 1. Representative horizontal acceleration peak values for the 1989 Loma Prieta earthquake recorded at Gilroy Array Station 1 in the North-South direction

Possible correlations between a_{max} and a_{av} , as well as $N(a_{max})$ and N_{tot} were examined. Fig. 2 shows that a_{max} and a_{av} are approximately directly proportional, with a ratio close to 1.87 being obtained. Regarding the correlation between the representative cycle at which the maximum acceleration was registered, $N(a_{max})$, and the total number of cycles, N_{tot}, Fig. 3 suggests that the location of the largest peaks within the earthquake's time history may vary significantly from earthquake to earthquake, with a tendency for this peak to occur between the first loading cycle, $N(a_{max}) = 1$, and $N(a_{max}) = 0.80\ N_{tot}$.

Based on these findings, and assuming, as a first approach, that shear stresses induced in a soil element at a certain depth from ground surface are proportional to the ground acceleration (e.g. Seed and Idriss 1971; Ishihara and Yasuda 1975; Idriss and Boulanger 2006), a singular peak loading cycle with twice the amplitude of the remaining uniform loading cycles was considered. The location of the higher amplitude peak within the overall loading pattern, defined by the specific value of mean effective stress at which the loading regime is changed, p'_p, was varied in each test, in order to assess its influence on the liquefaction resistance of sand.

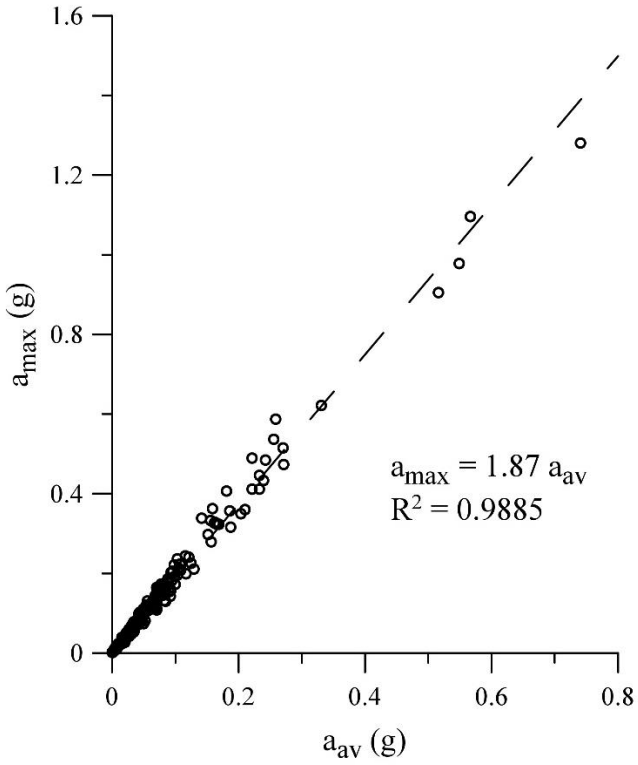

Fig. 2. Relationship between the maximum and average acceleration of real earthquake time histories

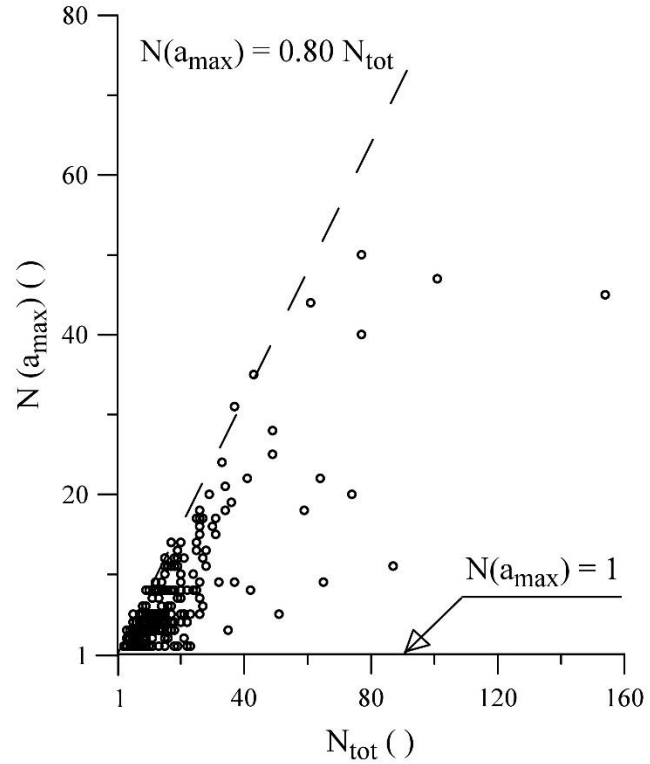

Fig. 3. Relationship between the cycle corresponding to the maximum peak acceleration and the total number of cycles of real earthquakes

As detailed in Table 1, in three of the tests – UCT 30/60/100, UCT 30/60/80 and UCT 30/60/50 – a peak loading cycle characterised by a peak value of deviatoric stress, q_p, of 60 kPa was applied when the mean effective stress, p'_p, reached 100, 80 and 50 kPa, respectively, with the remaining undrained loading consisting of cycles with a uniform deviatoric stress amplitude, q_u, of 30 kPa. Additionally, a test using uniform loading of 40 kPa, corresponding approximately to 0.65 q_p, as suggested by the methodology proposed by Seed and Idriss (1971) and Idriss and Boulanger (2006), – UCT 40 test – was performed.

As detailed later, in all of the aforementioned non-uniform loading tests, it was observed that the phase transformation (PT) line (Ishihara *et al.* 1975) (i.e. the line defining the transitory state at which the behaviour of sand changes from plastic contraction to plastic dilation) was initially crossed when the singular peak loading cycle was applied, leading to a very fast reduction of the mean effective stress in the subsequent loading cycles and, therefore, to the onset of liquefaction after few additional cycles. Consequently, in those tests, the early occurrence of the peak load was found to be unfavourable to the liquefaction resistance of sand. In order to investigate whether or not the peak loading cycle also presents a drastic influence on the liquefaction resistance of sand in situations where its application would not result in a premature crossing of the PT line, two additional tests were carried out, using smaller values of q_p = 45 kPa and q_u = 23 kPa – UCT 23/45/50 and UCT 23/45/80 tests. A test using a uniform loading of 30 kPa ($\approx$ 0.65 q_p of UCT 23/45/50 and UCT 23/45/80 tests) was also carried out – UCT 30 test.

Table 1. Summary of the initial conditions, loading characteristics and results of the undrained cyclic triaxial tests performed

Test ID †	e_0 ‡ ( )	p'_0 ‡ (kPa)	q_u (kPa)	q_p (kPa)	p'_p (kPa)	N_p ( )	N_{liq} § ( )	ΔW_{liq} § (kJ/m^3)	$\Delta W_{e;max\ liq}$ § (kJ/m^3)
UCT 23/45/50	0.665	100	23	45	50	61	81	2.26	1.97
UCT 23/45/80	0.664	100	23	45	80	27	88	2.14	2.20
UCT 30	0.670	100	30	–	–	–	66	2.29	2.64
UCT 30/60/50	0.666	100	30	60	50	39	43 (*)	(*)	(*)
UCT 30/60/80	0.671	100	30	60	80	8	11	2.35	1.93
UCT 30/60/100	0.670	100	30	60	100	1	3	2.06	1.66
UCT 40	0.670	100	40	–	–	–	13	2.20	1.45

† The designation identifies: 1) the type of drainage –U for undrained test; 2) the type of loading – CT for cyclic triaxial; 3) the uniform loading, q_u; 4) the peak loading, q_p, if applicable; 5) the mean effective stress at which the peak loading cycle was performed, if applicable.

‡ Post-consolidation values.

§ In the present study, the development of a residual pore water pressure ratio of 0.95 was considered to define the onset of liquefaction.

(*) The test had to be stopped after 43 loading cycles, before the sample had experienced liquefaction.

3. Experimental results and analysis

3.1. Sample response under similar loading conditions

Since a single method of sample preparation was used to produce samples with similar initial density and samples were consolidated to the same isotropic stress level, a similar undrained cyclic shear response is expected in all tests under similar loading conditions.

Fig. 4a show the accumulation of residual excess pore water pressure ratio, $(r_u)_{res}$, i.e. the ratio of excess pore water pressure corresponding to a null deviatoric stress, with the number of loading cycles, N, while Fig. 4b depicts the observed variation of double amplitude axial strain, ε_{DA}, with N. Except for the UCT 30/60/100 test, where the peak loading cycle was applied at the beginning of the test, and for UCT 30 and UCT 40 tests, where only uniform loading was used, the moment at which the peak loading cycle was applied in each test is clearly identified in this figure by a large filled square. It can be observed that the results obtained for the UCT 30 sample present a similar accumulation of residual pore water pressure and of axial strain with

number of loading cycles to those registered for the UCT 30/60/50 and UCT 30/60/80 tests, prior to the application of the peak load. Naturally, such similarity was suddenly interrupted by the occurrence of the peak loading cycle, as this triggered a very rapid increase of excess pore water pressure and axial strain accumulation.

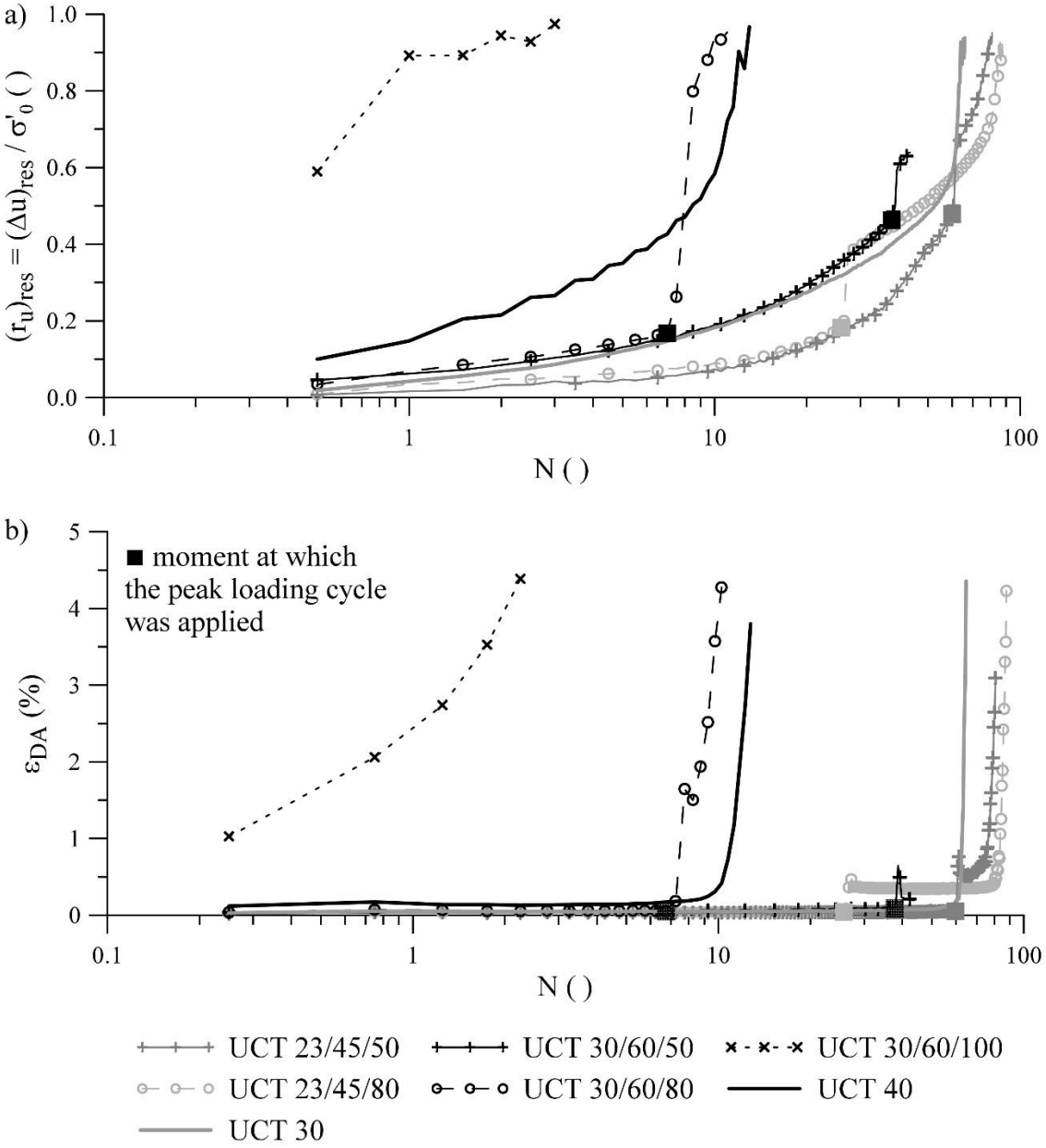

Fig. 4. Comparison of observed (a) residual pore water pressure build-up and (b) double amplitude axial strain with the number of cycles of loading

As expected, a different response was obtained for the UCT 30/60/100 test, since the peak load was applied in the first loading cycle, with the residual excess pore water pressure ratio being close to 0.90 just after that first cycle. Moreover, in the UCT 40 test, the larger deviatoric stress

amplitude led to higher rates of residual excess pore water pressure generation and of axial strain accumulation than those observed in the UCT 30, UCT 30/60/50 and UCT 30/60/80 tests, before any peak loading cycle was applied.

Likewise, the UCT 23/45/50 and UCT 23/45/80 tests presented a remarkably similar behaviour until the application of the peak loading cycle in the UCT 23/45/80 test (27^{th} loading cycle). As expected, these tests showed the lowest rate of accumulation of residual pore water pressure and double amplitude axial strain before peak load was applied, due to the smaller uniform deviatoric stress amplitude used (q_u = 23 kPa).

3.1.1. Number of loading cycles to the onset of liquefaction

It is usual to consider either the development of unit excess pore water pressure ratio (r_u = 1.0) or the observation of 5 % double amplitude axial strain (ε_{DA} = 5 %) as a condition to define the onset of liquefaction (also known as initial liquefaction) in laboratory testing (Ishihara 1996). As demonstrated later in this paper, when test results are interpreted using energy principles, a criterion based on the former quantity appears to be more adequate and, therefore, was adopted in the present study. Fig. 4 shows that, for the tests performed, the onset of liquefaction depends not only on the magnitude of loading (as inferred, for example, from the comparison between the results obtained for tests UCT 40 and UCT 30), but also on the loading pattern adopted in each test. More specifically, in the case of UCT 30/60/50, UCT 30/60/80 and UCT 30/60/100 tests, it can be observed that the later the singular peak loading cycle was applied, the greater the number of loading cycles required to trigger initial liquefaction, N_{liq}, as previously observed by Azeiteiro *et al.* (2012). Conversely, in the case of the UCT 23/45/50 and UCT 23/45/80 tests, a smaller difference between the number of loading cycles needed to reach initial liquefaction was observed, with the latter test requiring slightly more cycles (N_{liq} = 81 against 88, as indicated in Table 1), despite the earlier application of the peak load (N_p = 61 and 27, respectively, as also shown in Table 1). Indeed, it seems that the different impact of the location

of the peak loading cycle is related to whether or not the Phase Transformation (PT) line is crossed during its occurrence. As depicted in Fig. 5, while in the UCT 23/45/50, UCT 30/60/50 and UCT 30/60/80 tests, a reverse in the stress path can be observed during the extension part of the peak loading cycle, suggesting that the PT line has been crossed (Ishihara *et al.* 1975), this does not seem to occur in the UCT 23/45/80 test (Fig. 5a). Consequently, even if the larger shear stress oscillation imposed in the peak loading cycle results in a large increment of residual pore water pressure (Fig. 4a) and double amplitude axial strain (Fig. 4b), the reduction in mean effective stress upon load reversal is not as drastic in the UCT 23/45/80 test as it is in the UCT 23/45/50, UCT 30/60/50 and UCT 30/60/80 tests.

Moreover, Fig. 4 shows that the number of loading cycles needed to trigger liquefaction in the UCT 40 test (N_{liq} = 14) is smaller than that required in the UCT 30/60/50 test (more than 63 cycles), but larger than those needed in the UCT 30/60/80 and UCT 30/60/100 tests (11 and 3 cycles, respectively). This indicates that there is a substantial impact of the location of the peak loading cycle on the measured liquefaction strength, meaning that the laboratory evaluation of field liquefaction potential may need to take into account the irregularity of earthquake-induced shear stresses when stress-based analyses are performed.

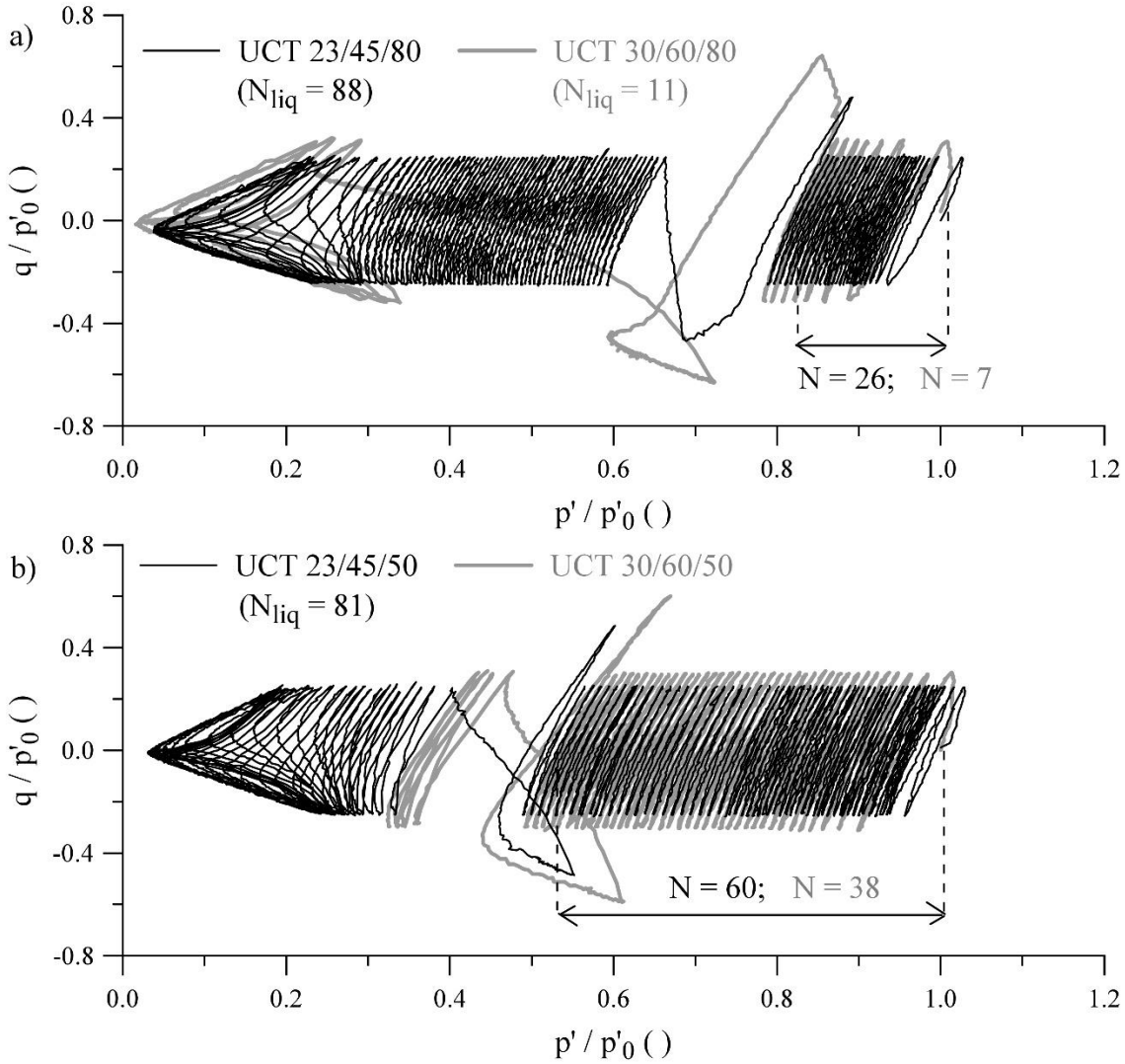

Fig. 5. Comparison of the stress path observed during (a) the UCT 23/45/80 and UCT 30/60/80 tests and (b) the UCT 23/45/50 and UCT 30/60/50 tests

3.2. Dissipated energy during undrained cyclic triaxial loading

In undrained triaxial shearing, the dissipated energy per unit volume (also known as unit energy, energy density or shear work per unit volume) per cycle, δW, can be determined using the area of the stress-strain hysteresis loop corresponding to that loading cycle. Since the stress-strain loops measured in each cycle of the conducted tests were not closed (Fig. 6a), the following methodology, outlined by Taborda *et al.* (2016), was adopted to estimate δW:

1) isolate each half-cycle stress-strain loop;
2) create a symmetric image of each half-cycle stress-strain loop about its centre;

3) centre each half-cycle stress-strain loop and its corresponding mirror image at the origin of the stress-strain space (i.e. move each half-loop in a way that its two tips are located at equal horizontal and vertical distances to the origin); an entire and closed stress-strain loop is defined by the original and the mirrored half-loop (Fig. 6b);
4) estimate the area enclosed by each closed loop using a trapezoidal approximation – Equation 1; and divide the obtained value by two in order to account only for the dissipated energy per unit volume in a half cycle.

[1] $$\delta W = \int \sigma \, d\varepsilon = \int_{k} q \, d\varepsilon_a \approx \sum_{i=1}^{k-1} \frac{1}{2} \left(q^{(i)} + q^{(i+1)} \right) \left(\varepsilon_a{}^{(i+1)} - \varepsilon_a{}^{(i)} \right)$$

where q is the deviatoric stress, ε_a is the axial strain and k is the total number of points in which the stress-strain loop is discretised.

For each of the performed tests, the accumulation of dissipated energy per unit volume, i.e. $\Delta W = \sum_{i=1}^{N} \delta W$, with the number of loading cycles, N, was determined (Fig. 7). It can be observed that a small amount of dissipated energy is accumulated during the earlier stages of loading, with a sharp increase of this quantity being measured as sand approaches liquefaction. It is also interesting to point out that, as expected, the accumulation of dissipated energy with the number of loading cycles (Fig. 7) follows a similar pattern to that described by the observed double amplitude axial strain (Fig. 4). Moreover, a clear jump in ΔW – N curves can be seen at the moment the peak loading cycle occurs.

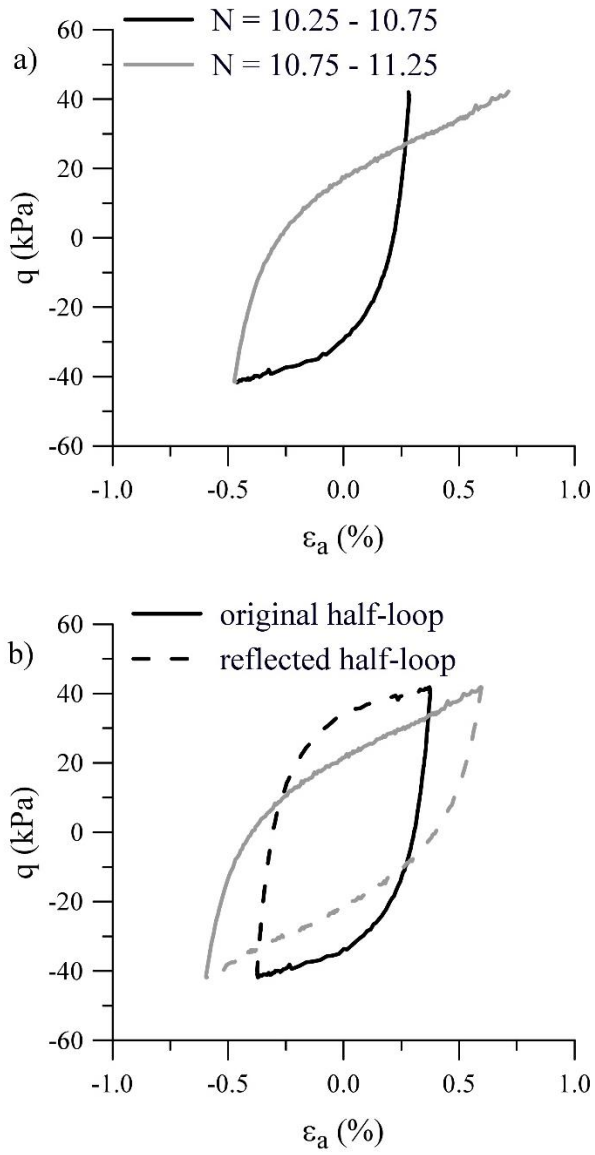

Fig. 6. Example of application of the methodology used to estimate the dissipated energy per unit volume (UCT 40 test): (a) original half-loops and (b) construction of closed loops using mirror images

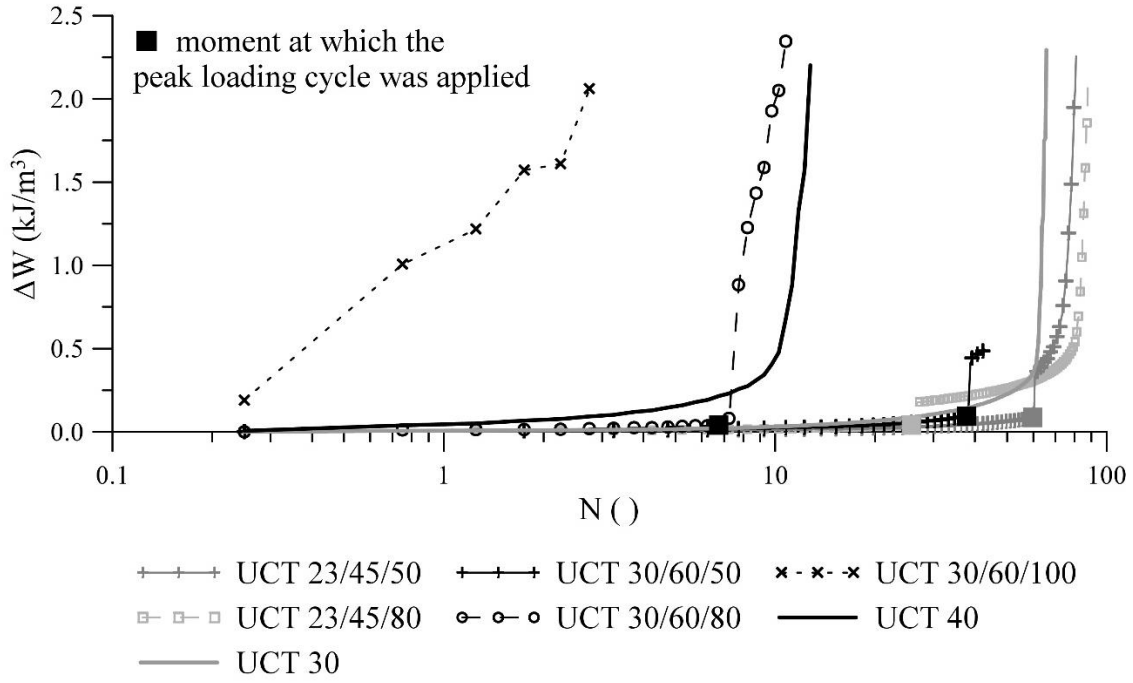

Fig. 7. Accumulation of dissipated energy per unit volume with the number of loading cycles

3.3. Excess pore water pressure generation as a function of dissipated energy

Fig. 8 presents the relationship between the dissipated energy per unit volume, ΔW, normalised by the post-consolidation isotropic effective stress (σ'_0 = 100 kPa), and the ratio of residual excess pore water pressure build-up, $(r_u)_{res} = (\Delta u)_{res} / \sigma'_0$. Although all samples have been consolidated to the same isotropic stress σ'_0, a normalisation of ΔW by σ'_0 was used to facilitate the comparison with other results published in the literature (see Table 2). Moreover, while $(\Delta u)_{res}$ was measured at the beginning and middle of each loading cycle (where the deviatoric stress is null), ΔW was estimated per each half-cycle and, therefore, between points corresponding to the maximum and minimum deviatoric stress. Thus, in order to compare these quantities, average values of residual pore water pressure were used – a procedure similar to that followed by Simcock *et al.* (1983). As shown in Fig. 8, similar curves were obtained for all conducted tests, which suggests that $(r_u)_{res} - \Delta W / \sigma'_0$ relationship is practically independent of the loading pattern imposed in each test. These results seem to confirm those previously obtained by Towhata and Ishihara (1985), who observed that $(r_u)_{res} - \Delta W / \sigma'_0$ relationship is

independent of the loading pattern applied in a torsional shear device (torsional shear, triaxial shear, a combination of both, etc.). Indeed, the obtained results also extend those obtained by Liang *et al.* (1995) and Polito *et al.* (2013). Based on regression analyses of element laboratory test results, both groups of authors concluded that the capacity energy, ΔW_{liq}, seems to be independent of using a uniform or an earthquake-type time series loading. The present experimental results suggest that not only ΔW_{liq} appears to be independent of the loading pattern used in each test (see Table 1), but also that a unique relationship between $(r_u)_{res}$ and $\Delta W / \sigma'_0$ is obtained for the entire loading history (i.e. from the earlier stages of loading to the moment liquefaction is triggered).

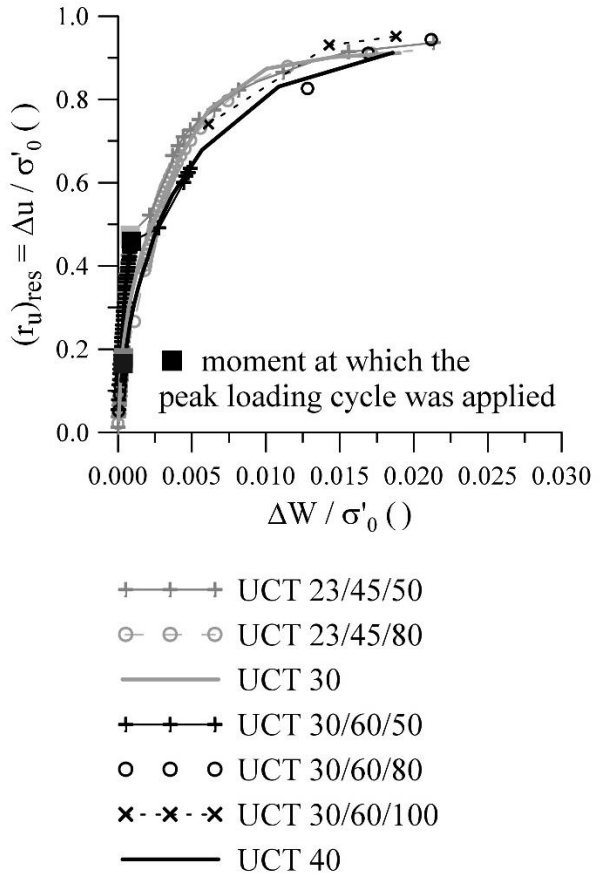

Fig. 8. Ratio of residual pore water pressure build-up as a function of the accumulation of dissipated energy per unit volume

As suggested by Liang *et al.* (1995), this may indicate that the laboratory evaluation of field liquefaction based on an energy-based method can be performed using uniform loading, rather

than using a complex earthquake-loading pattern. More specifically, if the seismic wave energy dissipated by a given layer of a soil deposit during a representative earthquake is adequately estimated, either by a wave propagation analysis or using a simplified procedure (see, for example, Davis and Berrill (1998), Dief and Figueroa (2007), Jafarian *et al.* (2011) or Kokusho and Suzuki (2012) for further details), then liquefaction susceptibility can be evaluated by comparing this value with the energy required to the onset of liquefaction, i.e. the capacity energy. This latter quantity can be obtained by performing laboratory tests on representative samples subjected to the *in situ* stress state and using, for simplicity, uniform cyclic loading, since its value has been shown to be independent from the adopted loading history (see Fig. 4). As discussed by Seed et al. (1975), the use of uniform cyclic loading for the laboratory evaluation of liquefaction potential presents two great advantages: 1) the testing equipment requirements to carry out the laboratory tests are reduced and 2) the obtained laboratory data can be used to assess the liquefaction potential of that soil layer for several design earthquakes. The unique $(r_u)_{res} - \Delta W / \sigma'_0$ relationship further suggests that if a random stress history of an earthquake motion is to be represented by an uniform cyclic stress history which causes similar effect on the soil, then an energy-based approach (e.g. Green and Terri 2005) for implementing the Palmgren–Miner cumulative damage hypothesis (Milner 1945) seems to be more appropriate than a stress-based approach (e.g. Seed *et al.* 1975).

It is also noteworthy that, for a given material, a good correlation between $(r_u)_{res}$ and $\Delta W / \sigma'_0$ exists. This conclusion applies not only to clean sands, but also to silty-sand mixtures (Polito *et al.* 2008; Baziar and Jafarian 2007; Baziar and Sharafi 2011) and clays (Cao and Law 1992), with each of the materials having its specific relationship. This further expands the applicability of energy-based approaches for the evaluation of liquefaction potential.

The present experimental data was subsequently compared with laboratory test results obtained for other sands reported in the literature (Table 2). In accordance with the conclusions drawn

by Law *et al.* (1990) and Dief and Figueroa (2007), Fig. 9 suggests that the $(r_u)_{res} - \Delta W / \sigma'_0$ relationship depends on soil type and/or test conditions. Therefore, if an energy-based method is to be employed to evaluate the liquefaction potential of a specific site, representative samples of that soil deposit should be tested in laboratory to evaluate its particular $(r_u)_{res} - \Delta W / \sigma'_0$ relationship.

Table 2. Characteristics of laboratory testing programmes where the $(r_u)_{res} - \Delta W / \sigma'_0$ relationship for sand was examined

Sand	Index properties of sand					Initial test cond.[§]		Apparatus	Reference
	D_{50} (mm)	C_U ( )	Particle shape	e_{min} ( )	e_{max} ( )	e_0 ( )	σ'_0 (kPa)		
Coimbra	0.28	1.6	sub-angular to angular	0.48	0.81	0.67	100.0	Triaxial	–
Toyoura	0.17	1.7	sub-angular to angular	0.6	0.98	0.79-0.83	294.0	Torsional shear	Towhata and Ishihara (1985)
Fujian	0.40	1.6	(*)	0.55	0.86	0.65	150.0	Triaxial	Law *et al.* (1990)
Silica 60	0.22	(*)	(*)	0.63	1.10	0.72, 0.87	186.2	Triaxial	Okada and Nemat-Nasser (1994)
Reid Bedford	0.26	(*)	(*)	0.59	0.85	0.70	124.1	Torsional shear	Liang (1995)
Futtsu beach	0.19	1.9	sub-rounded	0.68	1.08	0.80, 0.88, 0.96	98.0	Triaxial	Kokusho (2013)
Hostun	0.33	1.4	sub-angular to angular	0.66	1.00	0.83	80.0	Triaxial	Azeiteiro *et al.* (2015)

[§] All tests were performed on isotropically consolidated samples; (*) This information is not provided in the reference.

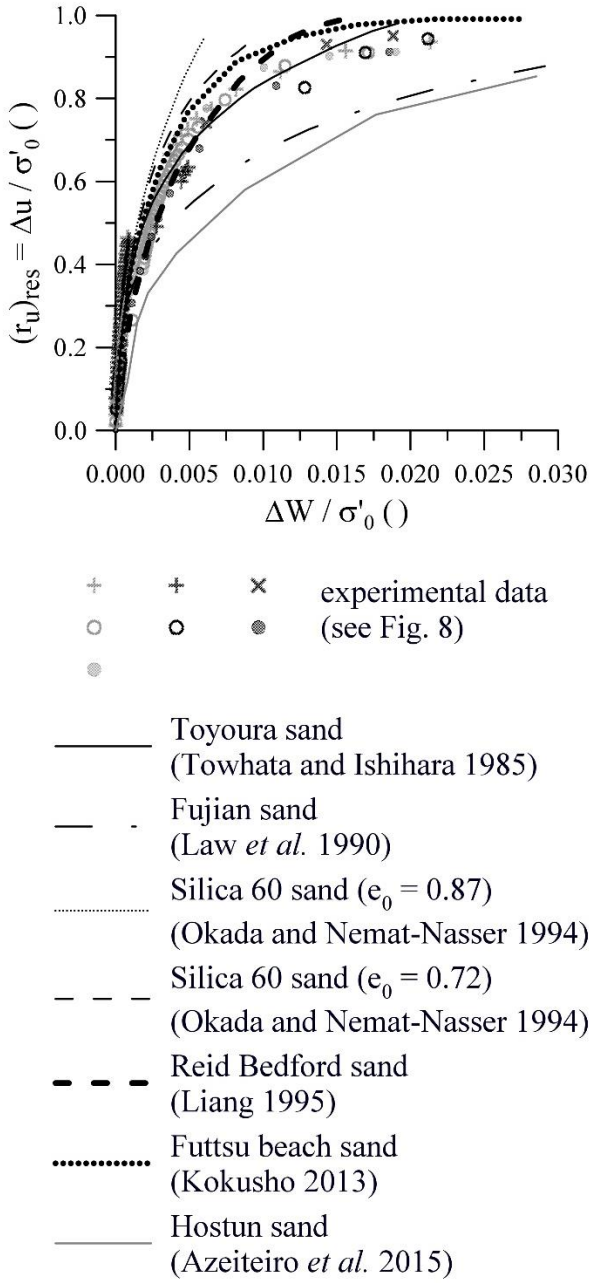

Fig. 9. Comparison of the $(r_u)_{res} - \Delta W/\sigma'_0$ relationship obtained in the present study with those obtained in different laboratory test programmes

3.4. Observed double amplitude axial strain as a function of dissipated energy

In contrast to the unique relationship between $(r_u)_{res}$ and $\Delta W / \sigma'_0$, the results shown in Fig. 10 suggest that the loading pattern has substantial influence on the relationship between $\Delta W / \sigma'_0$ and the double amplitude axial strain, ε_{DA}, observed during undrained cyclic triaxial loading. Moreover, it can be observed that, in general, as the number of loading cycles required to achieve a given level of ε_{DA} decreases (Fig. 4b), a higher average slope is obtained for the

$\Delta W / \sigma'_0 - \varepsilon_{DA}$ curve (Fig. 10), when comparing tests where a similar amplitude of loading was used – for example, UCT 30/60/80 and UCT 30/60/100 tests.

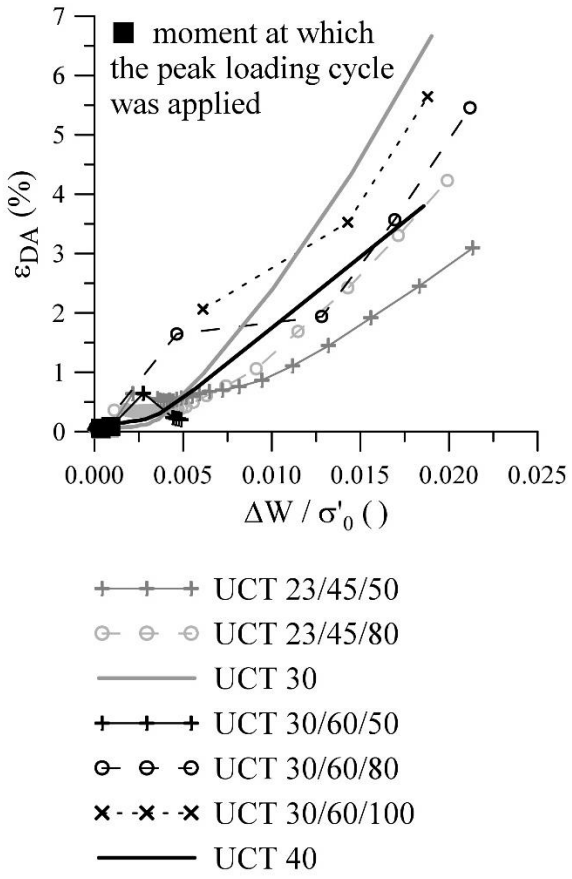

Fig. 10. Double amplitude axial strain as a function of the accumulation of dissipated energy per unit volume

4. Summary and conclusions

Undrained cyclic triaxial tests having a singular peak loading cycle of larger amplitude were carried out on similarly prepared air-pluviated samples of Coimbra sand to evaluate the effect of the location and magnitude of the largest peaks of earthquake-induced shear stresses on the liquefaction potential of sand. In order to use realistic loading in the experiments, the characteristics of real earthquakes were firstly examined. Based on the obtained results, three particular locations of the peak load were experimentally explored: at the beginning of shearing and when the mean effective stress reaches 80% and 50% of its initial value. Moreover, different shear stress amplitudes were used for both the peak loading cycle and uniform loading

pattern, in order to examine the influence of the crossing of the phase transformation line on the resistance of sand. Additionally, undrained cyclic triaxial tests using standard uniform loading were performed to evaluate the impact of using a simplified loading pattern in laboratory testing, rather than complex patterns more akin to those imposed during real earthquake motions.

The experimental results suggest that the number of cycles required to the onset of liquefaction depends not only on the magnitude of the imposed loading, but also on the loading pattern followed in that particular test. It was observed that the occurrence of an early peak load can either greatly reduce the liquefaction resistance or have only a minor effect, with the analysis of the registered stress paths suggesting that such substantial difference is related to whether or not the phase transformation line is crossed. Indeed, when the application of the peak loading cycle resulted in the crossing of the phase transformation line, a more detrimental effect on liquefaction resistance of sand was observed.

The results of these laboratory tests were further investigated using energy concepts, to examine whether or not energy-based evaluation of field liquefaction potential also need to incorporate the irregularity of loading. The accumulation of dissipated energy per unit volume, ΔW, was estimated using the recorded stress-strain responses. Possible correlations with the observed ratio of residual excess pore water pressure build-up, $(r_u)_{res}$, and double amplitude axial strain, ε_{DA}, were explored. It was found that a unique relationship between $\Delta W / \sigma'_0$ and $(r_u)_{res}$ appears to exist, being independent of both amplitude and location of peak loading cycle. Furthermore, similar results were obtained when using uniform or non-uniform loading. This suggests that standard cyclic tests using uniform loading can be used for realistic energy-based evaluation of field liquefaction potential.

5. Acknowledgements

This work was supported by FCT – Fundação para a Ciência e Tecnologia, Portugal (research project FCOMP-01-0124-FEDER-009790 and grant no. SFRH/BD/84656/2012), as part of the financial programme POPH – Programa Operacional Potencial Humano.

6. References

Ambraseys, N., Smit, P., Douglas, J., Margaris, B., Sigbjornsson, R., Olafsson, S., Suhadolc, P., and Costa, G. 2004. Internet-Site for European Strong-Motion Data. Bollettino di Geofisica Teorica e Applicata, **45**(3): 113-129. See http://www.isesd.hi.is/ESD_Local/frameset.htm. Accessed 24/08/2015.

Ancheta, T.D., Darragh, R.B., Stewart, J.P., Seyhan, E., Silva, W.J., Chiou, B.S.-J., Wooddell, K.E., Graves, R.W., Kottke, A.R., Boore, D.M., Kishida, T., and Donahue, J.L. 2013. PEER NGA-West2 Database. PEER Report No. 2013/03, Pacific Earthquake Engineering Research Center, University of California, Berkeley, USA, 134. See http://ngawest2.berkeley.edu/. Accessed 24/08/2015.

Aoi, S., Kunugi, T., and Fujiwara, H. 2004. Strong-motion Observation Networks of NIED: K-NET and KiK-net. Journal of Japan Association for Earthquake Engineering, **4**(3), 65–74. See http://www.kyoshin.bosai.go.jp/. Accessed 31/03/2013.

Archuleta, R., Steidl, J. and Squibb, M. 2004. The COSMOS Virtual Data Center. *In* Proceedings of the 13th World Conference on Earthquake Engineering, Vancouver, B.C., Canada, 1-6 August 2004, paper no. 1566. See http://strongmotioncenter.org/vdc/. Accessed 24/08/2015.

Azeiteiro, R.N., Marques, V.D., and Coelho, P.A.L.F. 2012. Effect of singular peaks in uniform cyclic loading on the liquefaction resistance of a sand. *In* Proceedings of the 2nd International Conference on Performance-Based Design in Earthquake Geotechnical Engineering, Taormina, Italy, 28-30 May 2012, paper no. 6.13.

Azeiteiro, R.N., Coelho, P.A.L.F., Taborda, D.M.G., and Grazina, J.C. 2015. Dissipated energy in undrained cyclic triaxial tests. *In* Proceedings of the 6th International Conference on Earthquake Geotechnical Engineering, Christchurch, New Zealand, 1-4 November 2015, paper no. 220.

Baziar, M.H., and Jafarian, Y. 2007. Assessment of liquefaction triggering using strain energy concept and ANN model: Capacity Energy. Soil Dynamics and Earthquake Engineering, **27**: 1056–1072. doi:10.1016/j.soildyn.2007.03.007.

Baziar, M.H., and Sharafi, H. 2011. Assessment of silty sand liquefaction potential using hollow torsional tests – An energy approach. Soil Dynamics and Earthquake Engineering, 31: 857–865. doi:10.1016/j.soildyn.2010.12.014.

Berrill, J.B., and Davis, R.O. 1985. Energy dissipation and seismic liquefaction of sands: revised model. Soils and Foundations, **25**(2): 106–118. doi: 10.3208/sandf1972.25.2_106.

Bishop, A.W., and Wesley, L.D. 1975. A hydraulic triaxial apparatus for controlled stress path testing. Géotechnique, **25**(4): 657–670. doi: 10.1680/geot.1975.25.4.657.

Cao, Y.L., and Law, K.T. 1992. Energy dissipation and dynamic behaviour of clay under cyclic loading. Canadian Geotechnical Journal, **29**: 103-111. doi: 10.1139/t92-011.

Davis, R.O., and Berrill, J.B. 1982. Energy dissipation and seismic liquefaction in sands. Earthquake Engineering and Structural Dynamics, **10**(1): 59–68. doi: 10.1002/eqe.4290100105.

Davis, R.O., and Berrill, J.B. 1998. Site-specific prediction of liquefaction. Géotechnique, **48**(2): 289–293. doi: 10.1680/geot.1998.48.2.289.

Dief, H. M., and Figueroa, J. L. 2007. Liquefaction assessment by the unit energy concept through centrifuge and torsional shear tests. Canadian Geotechnical Journal, **44**: 1286–1297. doi: 10.1139/T07-059.

Dobry, R., Ladd, R.S., Yokel, F.Y., Chung, R.M., and Powell, D. 1982. Prediction of pore water pressure buildup and liquefaction of sands during earthquakes by the cyclic strain method. NBS Building science series 138, National Bureau of Standards, U. S. Department of Commerce, U. S. Governmental Printing Office, Washington, D.C.

Figueroa, J.L., Saada, A.S., Liang, L., and Dahisaria, N.M. 1994. Evaluation of soil liquefaction by energy principles. Journal of Geotechnical Engineering, **120**(9): 1554–1569. doi: 10.1061/(ASCE)0733-9410(1994)120:9(1554).

Green, R.A., and Terri, G.A. 2005. Number of equivalent cycles concept for liquefaction evaluations-revisited. Journal of Geotechnical and Geoenvironmental Engineering, 131(4): 477–488. doi: 10.1061/(ASCE)1090-0241(2005)131:4(477).

Haddadi, H., Shakal, A., Stephens, C., Savage, W., Huang, M., Leith, W., Parrish, J., Borcherdt, R. 2008. Center for Engineering Strong-Motion Data (CESMD). *In* Proceedings of the 14th World Conference on Earthquake Engineering, Beijing, China, 12-17 October 2008, paper no. 1566. See http://www.strongmotioncenter.org/. Accessed 24/08/2015.

Hancock, J., and Boomer, J. 2005. The effective number of cycles of earthquake ground motion. Earthquake Engineering and Structural Dynamics, **34**: 637–664. doi: 10.1002/eqe.437.

Idriss, I.M., and Boulanger, R.W. 2006. Semi-empirical procedures for evaluating liquefaction potential during earthquakes. Soil Dynamics and Earthquake Engineering, **26**: 115–130. doi: 10.1016/j.soildyn.2004.11.023.

Ishihara, K. 1996. Soil behaviour in earthquake geotechnics. Oxford engineering series, Oxford, Oxford University Press.

Ishihara, K., and Yasuda, S. 1975. Sand liquefaction in hollow cylinder torsion under irregular excitation. Soils and Foundations, **15**(1): 45–59. doi: 10.3208/sandf1972.15.45.

Ishihara, K., Tatsuoka, F., and Yasuda, S. 1975. Undrained deformation and liquefaction of sand under cyclic stresses. Soils and Foundations, **15**(1): 29–44. doi: 10.3208/sandf1972.15.29.

Jafarian, Y., Sadeghi Abdollahi, A., Vakili, R., Baziar, M.H., and Noorzad, A. 2011. On the efficiency and predictability of strain energy for the evaluation of liquefaction potential: a numerical study. Computers and Geotechnics, **38**(6): 800–808. doi: 10.1016/j.compgeo.2011.06.001.

Jorge, C., and Vieira, A.M. 1997. Liquefaction potential assessment – Application to the Portuguese territory and to the town of Setúbal. *In* Seismic Behaviour of Ground and Geotechnical Structures. *Edited by* Pedro S. Seco e Pinto, CRC Press/Balkema, Rotterdam, Netherlands, pp. 33–43.

Kokusho, T. 2013. Liquefaction potential evaluations: energy-based method versus stress-based method. Canadian Geotechnical Journal, **50**: 1088–1099. doi: 10.1139/cgj-2012-0456.

Kokusho, T. and Suzuki, T. 2011. Energy flow in shallow depth based on vertical array records during recent strong earthquakes. Soil Dynamics and Earthquake Engineering, **31**: 1540–1550. doi: 10.1016/j.soildyn.2011.06.003.

Law, K.T., Cao, Y.L., and He, G.N. 1990. An energy approach for assessing seismic liquefaction potential. Canadian Geotechnical Journal, **27**: 320–329. doi: 10.1139/t90-043.

Liang, L. 1995. Development of an energy method for evaluating the liquefaction potential of a soil deposit. Ph.D. thesis. Department of Civil Engineering, Case Western Reserve University, Cleveland, Ohio.

Liang, B.L., Figueroa, J.L, and Saada, A.S. 1995. Liquefaction under random loading: unit energy approach. Journal of Geotechnical Engineering, **121**(11): 776–781. doi: 10.1061/(ASCE)0733-9410(1995)121:11(776).

Miner, M.A. 1945. Cumulative damage in fatigue. Trans. ASME 67, A159–A164.

Nemat-Nasser, S., and Shokooh, A. 1979. A unified approach to densification and liquefaction of cohesionless sand in cyclic shearing. Canadian Geotechnical Journal, **16**: 659–678. doi: 10.1139/t79-076.

Okada, N., and Nemat-Nasser, S. 1994. Energy dissipation in inelastic flow of saturated cohesionless granular media. Géotechnique, **44**(1): 1–19. doi: 10.1680/geot.1994.44.1.1.

Polito, C.P., Green, R.A., and Lee, J. 2008. Pore pressure generation models in sands and silty soils during cyclic loading. Journal of Geotechnical and Geoenvironmental Engineering, **134**(10): 1490–1500. doi: 10.1061/(ASCE)1090-0241(2008)134:10(1490).

Polito, C., Green, R.A., Dillon, E. and Sohn, C. 2013. Effect of load shape on relationship between dissipated energy and residual excess pore pressure generation in cyclic triaxial tests. Canadian Geotechnical Journal, **50**: 1118–1128. doi: 10.1139/cgj-2012-0379.

Santos, J.A., Gomes, R.C., Lourenço, J.C., Marques, F., Coelho, P.A.L.F., Azeiteiro, R.N., Marques, V.D., Santos, L.A., Viana da Fonseca, A., Soares, M., Abreu, É., and Taborda, D.M.G. 2012. Coimbra Sand – round robin tests to evaluate liquefaction resistance. *In* Proceedings of the 15th World Conference on Earthquake Engineering, Lisbon, Portugal, 24-28 September 2012, paper no. 4933.

Seed, H.B., Idriss, I.M., Makdidi, F. and Nanerjee, N. 1975. Representation of irregular stress time histories by equivalent uniform stress series in liquefaction analyses. Report No. EERC 75–29, Earthquake Engineering Research Center, University of California, Berkeley.

Seed, H.B., and Idriss, I.M. 1971. Simplified procedure for evaluating soil liquefaction potential. Journal of the Soil Mechanics and Foundations Division, **97**(9): 1249–1273.

Simcock, K.J., Davis, R.O., Berrill, J.B., and Mullenger, G. 1983. Cyclic triaxial tests with continuous measurement of dissipated energy. Geotechnical Testing Journal, **6**(1): 35–39. doi: 10.1520/GTJ10822J.

Taborda, D.M.G., Potts, D.M. and Zdradković, L. 2016. On the assessment of energy dissipated through hysteresis in finite element analysis. Computers and Geotechnics, **71**: 180–194. doi:10.1016/j.compgeo.2015.09.001.

Towhata, I., and Ishihara, K. 1985. Shear work and pore water pressure in undrained shear. Soils and Foundations, **25**(3): 73–85. doi: 10.3208/sandf1972.25.3_73

7. List of symbols

a_{av}	average of the representative values of the acceleration time-history of a ground motion (analysis of real earthquake records);
a_{max}	maximum peak acceleration of a ground motion (analysis of real earthquake records);
C_u	uniformity coefficient;
D_{50}	mean grain size;
e	void ratio;
e_0	void ratio before shearing;
e_{min}, e_{max}	minimum and maximum void ratios, respectively;
g	acceleration of gravity (≈ 9.81 m/s^2);
G_s	density of soil particles;
k	total number of points in which a stress-strain loop is discretised;
M_w:	moment magnitude;
N	number of loading cycles;
N_{liq}	number of loading cycles required to the onset of liquefaction;
N_p	number of the loading cycle at which the peak load was applied;
N_{tot}	total number of representative cycles of the acceleration time-history of a ground motion (analysis of real earthquake records);
$N(a_{max})$	representative cycle at which the maximum acceleration occurred (analysis of real earthquake records);
p'	mean effective stress;

p'_0, p'_p	mean effective stress after consolidation and at the moment the peak loading cycle was applied, respectively;
q	deviatoric stress or deviatoric stress oscillation (two-way symmetrical stress reversal loading);
q_p, q_u	deviatoric stress oscillation of the peak loading cycle and of the remaining uniform loading, respectively;
q_{max}	maximum deviatoric stress;
r_u	excess pore water pressure ratio;
$(r_u)_{res}$	residual excess pore water pressure ratio (i.e. corresponding to zero deviatoric stress);
α:	azimuth of a ground motion, i.e. the angle from North to the orientation of the sensor component, in clockwise direction.
δW	dissipated energy per unit volume per cycle;
Δu	excess pore water pressure;
$(\Delta u)_{res}$	excess pore water pressure corresponding to zero deviatoric stress;
ΔW	accumulation of dissipated energy per unit volume;
ΔW_{liq}	accumulation of dissipated energy per unit volume until the onset of liquefaction (capacity energy);
ε_a	axial strain;
$\varepsilon_{a;\,max}$	maximum amplitude of axial strain;
ε_{DA}	double amplitude axial strain;
σ'_0	isotropic effective stress after consolidation.

Appendix

Analyses of real earthquake motions were performed to study the location and magnitude of the largest peak loading cycle within the loading history.

Table A.1. Location and magnitude of the largest peak loading cycle in real earthquake's time histories

Earthquake	Station	Database†	M_w ( )	α (^{o})	$\lvert a_{max}\rvert$ (g)	$N(a_{max})$ ( )	N_{tot} ( )	$\lvert a_{av}\rvert$ (g)
1935 Helena, Montana	Helena Federal Build, MT, USA	PEER	6.0	0	0.047	2	4	0.023
				90	0.041	1	2	0.026
1957 San Francisco	Golden Gate Park, CA, USA	PEER	5.3	10	0.095	4	7	0.047
				100	0.112	4	6	0.074
1970 Lytle Creek	Allen Ranch Miller Canyon, CA, USA	PEER	5.3	95	0.071	3	8	0.040
				185	0.050	8	9	0.032
1971 San Fernando	Allen Ranch Miller Canyon, CA, USA	PEER	6.6	95	0.020	2	16	0.010
				185	0.015	1	23	0.008
	Lake Hughes Sta. 4, CA, USA			111	0.192	8	13	0.104
				201	0.153	8	18	0.077
	Lake Hughes Sta. 9, CA, USA			21	0.157	4	17	0.085
				291	0.134	7	13	0.074
	Pasadena, CA, USA			180	0.089	8	24	0.048
				270	0.202	8	12	0.100
	Santa Anita dam, CA, USA			3	0.151	18	34	0.076
				273	0.212	11	15	0.107
1972 Kefalonia island	Kefalonia, Greece	ISESD	5.6	0	0.122	8	10	0.070
				90	0.174	5	11	0.086
1974 Hollister	Gilroy Array Sta. 1, CA, USA	PEER	5.1	157	0.105	6	8	0.059
				247	0.132	3	7	0.070
1975 Oroville	Oroville Seism. Sta., CA, USA	PEER	5.9	37	0.092	4	10	0.048
				307	0.072	1	11	0.046
1976 Friuli	Ambiesta dam, Tolmezzo, Italy	ISESD	6.5	0	0.357	1	6	0.207
				90	0.316	1	6	0.230
1978 Albstadt	Jungingen, Germany	ISESD	4.2	L (*)	0.043	2	4	0.029
				T (*)	0.053	1	7	0.026
1978 Southern Calabria	Ferruzzano, Italy	ISESD	5.2	0	0.076	1	10	0.038
				90	0.078	1	11	0.043
1978 Gulf of Patti, Sicily	Milazzo, Italy	ISESD	6.0	0	0.068	4	14	0.032
				90	0.074	5	14	0.036
1978 Tabas, Iran	Dayhook, Iran	PEER	7.4	L (*)	0.328	7	19	0.169
				T (*)	0.406	3	10	0.184
1979 Montenegro	Pomorska Skola, Dubrovnik, Croatia	ISESD	6.9	0	0.066	8	22	0.034
				90	0.075	3	13	0.038
1979 Dead Sea (**)	Kefar Etziyon, Israel	ISESD	5.1	90	0.010	3	13	0.005

Earthquake	Station	Database†	M_w ( )	α (°)	$\|a_{max}\|$ (g)	$N(a_{max})$ ( )	N_{tot} ( )	$\|a_{av}\|$ (g)
1979 Coyote Lake	Coyote Lake dam, CA, USA	PEER	5.7	160	0.157	2	9	0.083
				250	0.279	2	4	0.157
	Gilroy Array Sta. 1, CA, USA			230	0.103	12	15	0.053
				320	0.132	3	9	0.066
1979 Bucak	Bucak, Turkey	ISESD	5.9	0	0.016	2	5	0.009
				90	0.013	1	7	0.008
1979 Valnerina	Cascia, Italy	ISESD	5.8	0	0.154	1	18	0.096
				90	0.205	2	8	0.108
1979 Imperial Valley	Cerro Prieto, Mexico	PEER	6.5	147	0.168	5	51	0.097
				237	0.157	25	49	0.092
	Superstition Mtn, CA, USA			45	0.109	5	13	0.054
				135	0.195	3	8	0.112
1980 Livermore A	APEEL 3E, CA, USA	PEER	5.8	146	0.072	3	7	0.040
				236	0.057	3	13	0.033
1980 Livermore B	APEEL 3E, CA, USA	PEER	5.4	146	0.053	2	3	0.037
				236	0.028	3	9	0.016
1980 Anza	Anza Array, Terwilliger Valley, CA, USA	PEER	5.2	45	0.131	4	5	0.088
				135	0.081	2	7	0.056
1980 Anza	Anza Array, Pinyon Flat Obs., CA, USA	PEER	5.2	45	0.110	4	8	0.062
				135	0.131	2	5	0.067
1980 Victoria, Mexico	Cerro Prieto, Mexico	PEER	6.3	45	0.621	4	5	0.357
				315	0.587	3	4	0.291
1980 Irpinia	Bagnoli Irpino, Italy	ISESD	6.9	0	0.139	8	17	0.073
				90	0.181	2	7	0.110
1981 Westmorland	Superstition Mtn, CA, USA	PEER	5.9	45	0.071	3	9	0.042
				135	0.116	3	7	0.062
1981 NE of Banja Luka	Seism. Sta. Banja Luka, Bosnia & Herzegovina	ISESD	5.7	0	0.074	1	8	0.044
				90	0.075	5	9	0.043
1983 Coalinga	Slack Canyon, CA, USA	PEER	6.4	45	0.166	3	5	0.097
				315	0.153	3	7	0.077
1983 Biga	Edincik, Turkey	ISESD	6.1	0	0.049	6	16	0.027
				90	0.050	7	11	0.026
1983 Ierissos	Ouranoupolis, Greece	ISESD	5.1	L (*)	0.083	2	6	0.048
				T (*)	0.130	3	4	0.091
1983 Erzurum	Erzurum, Turkey	ISESD	6.6	0	0.028	6	14	0.014
				90	0.017	5	20	0.010
1984 Morgan Hill	Gilroy Array Sta. 1, CA, USA	PEER	6.2	230	0.069	20	29	0.037
				320	0.098	5	14	0.046
1984 Umbria	Gubbio, Italy	ISESD	5.6	0	0.051	3	16	0.026
				90	0.067	3	12	0.038
1984 Lazio Abruzzo	Atina, Italy	ISESD	5.9	0	0.100	4	11	0.049
				90	0.110	3	7	0.054
1984 Izmir	Foça, Izmir, Turkey	ISESD	5.1	0	0.012	1	5	0.007
				90	0.013	1	4	0.008
1984 Granada	Presa de Béznar, Spain	ISESD	4.9	L (*)	0.015	4	12	0.008
				T (*)	0.018	5	10	0.010

Earthquake	Station	Database†	M_w ( )	α (^{o})	$\lvert a_{max} \rvert$ (g)	$N(a_{max})$ ( )	N_{tot} ( )	$\lvert a_{av} \rvert$ (g)
1984 Jezreel Valley	Haifa, Israel	ISESD	5.3	0	0.040	5	7	0.026
				90	0.047	3	7	0.027
1984 Kranidia	Prefecture, Kozani, Greece	ISESD	5.5	L (*)	0.036	2	4	0.021
				T (*)	0.026	1	9	0.014
1984 Messinia peninsula	Town Hall Pelekanada, Greece	ISESD	3.7	L (*)	0.028	3	10	0.015
				T (*)	0.031	2	5	0.018
1985 Anchialos	Prefecture, Lamia, Greece	ISESD	5.6	L (*)	0.020	8	13	0.011
				T (*)	0.016	4	14	0.008
1985 Gulf of Kyparissia	Agriculture Bank, Kyparissia, Greece	ISESD	5.4	L (*)	0.021	6	17	0.012
				T (*)	0.039	3	4	0.022
1985 Drama	Prefecture, Kavala, Greece	ISESD	5.2	L (*)	0.053	4	11	0.026
				T (*)	0.037	4	22	0.020
1985 Nahanni	Site 1, Canada	PEER	6.8	10	0.978	5	7	0.608
				280	1.096	5	5	0.609
	Site 2, Canada			240	0.489	2	6	0.235
				330	0.313	2	15	0.173
	Site 3, Canada			270	0.148	22	64	0.074
				360	0.139	11	87	0.074
1986 Skydra-Edessa	Cultural Center, Veria, Greece	ISESD	5.3	L (*)	0.010	8	17	0.006
				T (*)	0.018	3	7	0.009
1986 Hollister	SAGO South, CA, USA	PEER	5.5	205	0.044	3	9	0.025
				295	0.090	2	5	0.047
1986 Golbasi	Golbasi, Turkey	ISESD	6.0	0	0.039	2	6	0.018
				90	0.055	3	8	0.030
1986 North Palm Springs	Anza Array, Red Mtn., CA, USA	PEER	6.1	270	0.103	5	14	0.057
				360	0.129	2	8	0.077
	Murrieta Hot Springs, CA, USA			0	0.053	5	21	0.027
				90	0.049	5	23	0.027
	Anza Array, S. Rosa Mtn., CA, USA			270	0.106	8	18	0.054
				360	0.103	14	20	0.046
	Poppet Flats Rd., Banning, CA, USA			0	0.139	3	13	0.077
				90	0.113	5	8	0.066
	Bergman Ranch Hemet Sta. B, CA, USA			0	0.070	10	24	0.034
				90	0.093	5	15	0.048
1986 Vrancea	Vrâncioaia, Romania	ISESD	7.2	0	0.084	4	11	0.042
				90	0.143	5	13	0.072
1986 Kalamata	Police Sta. Githio, Greece	ISESD	5.9	L (*)	0.006	14	17	0.004
				T (*)	0.007	8	17	0.004
1987 Gulf of Ierissos	Ouranoupolis, Greece	ISESD	4.1	L (*)	0.017	1	3	0.009
				T (*)	0.010	1	5	0.006
1987 Baja California	Cerro Prieto, Mexico	PEER	5.5	161	1.388	1	4	0.814
				251	0.890	3	4	0.602
1987 Mt. Vatnafjoll	Flagbjarnarholt, Iceland	ISESD	6.0	L (*)	0.031	3	7	0.016
				T (*)	0.035	5	9	0.021

Earthquake	Station	Database†	M_w ( )	α (°)	$\|a_{max}\|$ (g)	$N(a_{max})$ ( )	N_{tot} ( )	$\|a_{av}\|$ (g)
1987 Whittier Narrows A	Mt Wilson, CA, USA	PEER	6.0	0	0.123	19	36	0.062
				90	0.186	9	20	0.094
	Wonderland Ave, LA, CA, USA	PEER		75	0.039	11	16	0.022
				165	0.047	3	12	0.023
	Mill Creek Summit, CA, USA	PEER		0	0.089	4	20	0.047
				90	0.071	1	19	0.042
1987 Whittier Narrows B	Mt Wilson, CA, USA	PEER	5.3	0	0.158	1	4	0.090
				90	0.142	3	6	0.093
1987 Dodecanese islands	Seism. Sta. Archangelos, Greece	ISESD	5.3	235	0.032	3	6	0.018
				325	0.048	2	8	0.025
1987 NE coast of Rhodes Island	Military Camp, Rhodes, Greece	ISESD	5.1	L (*)	0.041	1	8	0.025
				T (*)	0.040	3	9	0.024
1987 SW coast of Peloponnese	Town Hall, Koroni, Greece	ISESD	5.2	L (*)	0.032	1	4	0.017
				T (*)	0.017	2	15	0.009
1988 SE of Tirana	Seism. Obs. Tirana, Albania	ISESD	5.9	0	0.113	7	11	0.065
				90	0.412	1	2	0.262
1988 Astakos	OTE Building, Amfilochia, Greece	ISESD	5.1	L (*)	0.033	5	13	0.019
				T (*)	0.016	5	15	0.008
1988 Agrinio	OTE Building, Amfilochia, Greece	ISESD	4.9	L (*)	0.056	3	5	0.034
				T (*)	0.039	6	8	0.024
1988 Rafina	Agriculture Bank, Kyparissia, Greece	ISESD	4.6	27	0.015	5	8	0.008
				297	0.025	2	5	0.013
1988 Aetolia-Acarnania	Valsamata, Greece	ISESD	5.3	L (*)	0.166	3	8	0.076
				T (*)	0.176	4	11	0.090
1988 Trilofon	Prefecture, Polygyros, Greece	ISESD	4.8	L (*)	0.015	4	10	0.008
				T (*)	0.014	1	7	0.007
1988 Spitak (**)	Avetisian Street, Yerevan, Armenia	ISESD	6.7	?	0.058	47	101	0.034
1989 Loma Prieta	Gilroy Array Sta. 1, CA, USA	PEER	6.9	0	0.411	3	9	0.215
				90	0.473	5	7	0.273
	Coyote Lake dam, CA, USA			195	0.151	14	17	0.084
				285	0.484	4	5	0.253
	City Hall, Monterey, CA, USA			0	0.073	13	28	0.035
				90	0.063	5	21	0.033
	SAGO Vault, CA, USA			270	0.036	14	25	0.021
				360	0.060	4	8	0.032
	APEEL 3E, CA, USA			0	0.078	5	13	0.043
				90	0.084	9	12	0.047
	Rincon Hill, SF, CA, USA			0	0.078	5	7	0.038
				90	0.092	1	4	0.051
	Yerba Buena Island, CA, USA			0	0.029	5	13	0.016
				90	0.068	2	5	0.037
1989 Chenoua	Bouzaréah, Algiers, ALgeria	ISESD	5.9	90	0.037	5	26	0.020
				180	0.035	5	26	0.021
1990 Reykjanes Peninsula	Foldaskoli, Reykjavik, Iceland	ISESD	4.7	L (*)	0.010	1	7	0.005
				T (*)	0.013	1	4	0.007

Earthquake	Station	Database†	M_w ( )	α (°)	$\|a_{max}\|$ (g)	$N(a_{max})$ ( )	N_{tot} ( )	$\|a_{av}\|$ (g)
1990 Vrancea	Vrâncioaia, Romania	ISESD	6.9	0	0.030	10	20	0.015
				90	0.024	4	8	0.011
1990 Filippias	Prefecture, Igoumenitsa, Greece	ISESD	5.5	L (*)	0.010	1	7	0.006
				T (*)	0.011	5	12	0.007
1990 Manjil	Zanjan, Iran	ISESD	7.4	L (*)	0.131	3	12	0.062
				T (*)	0.060	9	65	0.030
1990 Dinara Mt.	Ricice dam, Croatia	ISESD	5.5	0	0.120	4	20	0.068
				90	0.118	8	15	0.072
1990 Javakheti Highland	Akhalkalaki, Georgia	ISESD	5.4	0	0.033	3	7	0.018
				90	0.015	1	13	0.009
1990 Griva	Cultural Center, Veria, Greece	ISESD	6.1	L (*)	0.011	3	11	0.005
				T (*)	0.009	10	15	0.005
1991 Racha	Akhalkalaki, Georgia	ISESD	6.8	0	0.011	9	32	0.006
				90	0.007	21	34	0.004
1992 Landers	Morongo Valley, CA, USA	PEER	7.3	45	0.223	4	15	0.107
				135	0.164	11	18	0.078
1992 Big Bear	Snow Creek, CA, USA	PEER	6.5	90	0.164	17	31	0.077
				180	0.119	40	77	0.056
	Poppet Flats Rd., Banning, CA, USA			90	0.059	15	31	0.029
				360	0.070	9	37	0.035
	Bergman Ranch Hemet Sta. B, CA, USA			90	0.076	24	33	0.038
				360	0.059	20	74	0.031
	Rancho Cucamonga, CA, USA			90	0.051	17	27	0.026
				360	0.032	16	30	0.016
1992 Wutöschingen	Beringen, Switzerland	ISESD	3.7	0	0.006	3	7	0.003
				90	0.005	3	8	0.003
1993 Coast of Filiatra	OTE Building, Kyparissia, Greece	ISESD	5.2	L (*)	0.019	2	21	0.010
				T (*)	0.028	8	14	0.016
1993 Strait of Gibraltar	Refugio de la Plaza, Adra, Spain	ISESD	5.2	0	0.024	2	3	0.017
				90	0.026	2	4	0.019
1994 Northridge	Wonderland Ave, LA, CA, USA	PEER	5.3	95	0.048	3	5	0.033
				185	0.052	3	4	0.034
1994 Manisa	Demirtas, Turkey	ISESD	5.4	0	0.001	4	13	0.001
				90	0.001	3	12	0.001
1994 Firuzabad	Farashband, Iran	ISESD	5.9	247	0.015	17	26	0.008
				337	0.023	11	19	0.011
1994 Bitola	Cultural Center, Florina, Greece	ISESD	6.1	257	0.081	4	9	0.041
				347	0.073	2	7	0.050
1995 Kobe	Kakogawa, Japan	PEER	6.9	0	0.240	7	20	0.136
				90	0.324	8	17	0.177
1995 Igoumenitsa	Prefecture, Igoumenitsa, Greece	ISESD	3.8	0	0.019	3	5	0.010
				90	0.015	3	6	0.009
1995 Arnaia	Prefecture, Kavala, Greece	ISESD	5.3	87	0.009	4	18	0.005
				357	0.009	5	13	0.005
1995 Kozani	Prefecture, Kozani, Greece	ISESD	6.5	252	0.142	8	16	0.079
				342	0.208	3	9	0.116

Earthquake	Station	Database†	M_w ( )	α (°)	$\|a_{max}\|$ (g)	$N(a_{max})$ ( )	N_{tot} ( )	$\|a_{av}\|$ (g)
1995 Kolpos Ierissou	Prefecture, Polygyros, Greece	ISESD	4.2	238	0.011	2	9	0.006
				328	0.027	1	3	0.021
1995 Várpalota	Bodajk, Hungary	ISESD	3.8	L (*)	0.003	2	11	0.002
				T (*)	0.003	2	9	0.001
1996 Rhodes island	Military Camp, Rhodes, Greece	ISESD	5.4	18	0.010	22	41	0.005
				288	0.010	28	49	0.005
1996 East of Kythira island	Elementary School, Ag. Nikolaos, Greece	ISESD	4.5	318	0.019	1	6	0.012
				228	0.030	1	4	0.016
1996 East of Kythira island	Elementary School, Ag. Nikolaos, Greece	ISESD	4.5	228	0.030	1	4	0.016
				318	0.019	1	6	0.012
1996 Mt. Hengill Area	Hospital, Selfoss, Greece	ISESD	4.3	L (*)	0.010	2	6	0.005
				T (*)	0.005	4	12	0.003
1996 East of Karpenisi	Prefecture, Karpenisi, Greece	ISESD	3.8	54	0.008	3	4	0.005
				324	0.013	2	4	0.009
1996 Chalkidike	Prefecture, Polygyros, Greece	ISESD	3.9	238	0.008	4	9	0.005
				328	0.011	3	8	0.006
1996 Tadmuriyah	Talkalakh, Syria	ISESD	5.5	0	0.003	3	17	0.001
				90	0.002	3	35	0.001
1997 Rivion	OTE Building, Amfilochia, Greece	ISESD	3.2	L (*)	0.012	2	4	0.008
				T (*)	0.017	1	3	0.010
1997 Ardakul	Khezri Dashtebayaz, Iran	ISESD	7.2	0	0.019	44	61	0.010
				90	0.022	8	42	0.011
1997 South of Rhodes	Military Camp, Rhodes, Greece	ISESD	4.6	54	0.016	4	12	0.008
				324	0.012	12	19	0.007
1997 Mt. Hengill Area	Church, Hveragerði, Iceland	ISESD	4.9	L (*)	0.172	2	3	0.100
				T (*)	0.072	3	5	0.043
1997 Kalamata	Town Hall, Koroni, Greece	ISESD	6.4	35	0.121	8	18	0.062
				305	0.117	12	27	0.066
1997 NW of Makrakomi	Prefecture, Karpenisi, Greece	ISESD	4.7	54	0.012	1	22	0.006
				324	0.015	11	17	0.009
1997 Itea	Prefecture, Karpenisi, Greece	ISESD	5.6	54	0.017	4	6	0.009
				324	0.015	1	8	0.009
1997 Strofades	Agriculture Bank, Kyparissia, Greece	ISESD	6.6	27	0.066	10	20	0.035
				297	0.074	12	21	0.037
1997 Kastrakion	OTE Building, Amfilochia, Greece	ISESD	4.1	L (*)	0.028	3	4	0.017
				T (*)	0.018	2	8	0.009
1998 Bovec, Slovenia	Piazza del Ferro, Gemona, Italy	ISESD	5.6	180	0.008	8	16	0.004
				270	0.010	17	25	0.005
1998 San Juan Bautista	SAGO Vault, CA, USA	PEER	5.2	270	0.091	4	5	0.051
				360	0.097	1	6	0.045
1999 Laffrey, Grenoble	Dolphin museum, Grenoble, France	ISESD	3.5	0	0.001	13	19	0.001
				90	0.001	15	26	0.001
1999 Chamoli	Gopeshwar, India	COSMOS VDC	6.6	20	0.360	1	3	0.211
				290	0.199	1	4	0.119
1999 Karebas	Maharlo, Iran	ISESD	6.2	130	0.013	5	11	0.007
				220	0.010	3	11	0.006

Earthquake	Station	Database†	M_w ( )	α (°)	$\|a_{max}\|$ (g)	$N(a_{max})$ ( )	N_{tot} ( )	$\|a_{av}\|$ (g)
1999 Izmit	Meteo. Sta., Izmit, Turkey	ISESD	7.6	0	0.161	4	22	0.092
				90	0.223	8	17	0.120
	Levent, Istanbul, Turkey	COSMOS VDC		90	0.036	13	25	0.019
				180	0.041	4	11	0.022
1999 Hector Mine	29 Palms, CA, USA	PEER	7.1	90	0.066	9	26	0.032
				360	0.067	6	27	0.031
1999 Düzce	Mudurnu, Turkey	ISESD	7.2	0	0.120	4	15	0.057
				90	0.053	16	26	0.030
1999 Cresta di Reit	Punt Dal Gall, Livigno, Italy	ISESD	4.9	0	0.011	3	11	0.006
				90	0.010	4	13	0.005
2001 Martigny	St. Maurice resvr, Switzerland	ISESD	3.5	L (*)	0.005	4	9	0.003
				T (*)	0.008	3	6	0.004
2001 Pasinler	Erzurum, Turkey	ISESD	5.4	0	0.020	3	14	0.011
				90	0.022	2	15	0.012
2001 Albula pass	Bergün, Switzerland	ISESD	2.4	0	0.008	1	2	0.005
				90	0.006	3	3	0.004
2002 Kerns	Kerns, Switzerland	ISESD	2.5	0	0.011	1	6	0.007
				90	0.023	2	5	0.014
2002 Tbilisi	Seism. Obs., Tbilisi, Georgia	ISESD	4.8	L (*)	0.058	2	5	0.032
				T (*)	0.108	1	2	0.078
2002 Gilroy	Fire Sta., SF, CA USA	PEER	4.9	50	0.009	2	9	0.005
				140	0.006	2	15	0.003
2002 Buin Zahra, Iran	Avaj, Qazvin, Iran	ISESD	6.5	L (*)	0.446	9	14	0.244
				T (*)	0.433	4	9	0.258
2003 Pülümür	Bingöl, Turkey	ISESD	6.0	0	0.007	13	19	0.004
				90	0.008	11	16	0.004
2003 Big Bear City	Tripp Flats Training, Anza, CA, USA	PEER	4.9	90	0.005	7	26	0.003
				360	0.008	8	15	0.004
2003 Bingöl	Bingöl, Turkey	ISESD	6.3	0	0.515	3	10	0.285
				90	0.297	4	11	0.177
2003 Bam	Ravar, Iran	PEER	6.6	L (*)	0.012	4	17	0.006
				T (*)	0.012	5	15	0.007
	Zarand, Iran			L (*)	0.012	5	12	0.006
				T (*)	0.013	11	17	0.008
2004 Kojur-Firoozabad	Gilvān, Iran	ISESD	6.3	60	0.037	4	13	0.019
				150	0.036	3	18	0.018
2004 Parkfield	Police Station, Greenfield, CA, USA	PEER	6.0	90	0.034	4	9	0.019
				360	0.024	8	20	0.013
	Slack Canyon, CA, USA			90	0.211	3	5	0.148
				360	0.349	2	5	0.220
2004 Leskovik	Seism. Sta., Leskovik, Albania	ISESD	5.4	L (*)	0.090	6	9	0.046
				T (*)	0.053	5	14	0.029
2008 Olfus	Hveragerði, Iceland	ISESD	6.3	L (*)	0.536	1	4	0.267
				T (*)	0.326	3	5	0.173

Earthquake	Station	Database†	M_w ( )	α (°)	$\|a_{max}\|$ (g)	$N(a_{max})$ ( )	N_{tot} ( )	$\|a_{av}\|$ (g)
2009 L'Aquilla	Gran Sasso, Italy	CESMD	6.3	90	0.148	31	37	0.082
				360	0.145	35	43	0.085
2010 Chile	Cerro Santa Lucia, Santiago, Chile	CESMD	8.8	90	0.338	11	28	0.149
				360	0.243	50	77	0.124
2010 El Mayor-Cucupah	Pinyon Flat, Anza, CA, USA	PEER	7.2	90	0.013	18	26	0.007
				360	0.014	12	18	0.007
	Poppet Flats Rd., Banning, CA, USA			90	0.009	5	11	0.005
				360	0.007	11	18	0.004
2010 Canterbury	Lyttelton Port Company, New Zealand	CESMD	7.0	80	0.225	8	15	0.129
				170	0.332	5	10	0.166
2011 Tōhoku	Haga, Japan	NIED	9.0	90	0.221	5	11	0.128
				360	0.168	5	17	0.104
2011 Eastern Turkey	Meteo. Sta., Muradiye, Turkey	CESMD	7.2	90	0.173	8	14	0.082
				360	0.182	7	20	0.092
2014 Iquique	Chusmiza, Chile	CESMD	8.2	90	0.236	18	59	0.106
				360	0.363	8	25	0.164
2015 Nepal	Kantipath, Kathmandu, Nepal	CESMD	7.8	90	0.158	1	5	0.099
				360	0.164	4	15	0.088

† Ground motion data was obtained from:

Center for Engineering Strong Motion Data (CESMD) – http://www.strongmotioncenter.org/ (Haddadi *et al.* 2008);

Consortium of Organizations for Strong Motion Observation Systems (COSMOS): the Strong Ground-Motion Virtual Data Center (VDC) – http://strongmotioncenter.org/vdc/ (Archuleta *et al.* 2004;)

Internet-Site for European Strong Motion Data (ISESD) – http://www.isesd.hi.is/ESD_Local/frameset.htm (Ambraseys *et al.*, 2004);

National Research Institute for Earth Science and Disaster Prevention (NIED): K-NET (Kyoshin network) and KiK-net (Kiban Kyoshin network) – http://www.kyoshin.bosai.go.jp/ (Aoi *et al.* 2004);

Pacific Earthquake Engineering Research (PEER) Center: NGA-West2 database – http://ngawest2.berkeley.edu/ (Ancheta *et al.* 2013).

(*) The only information provided is: longitudinal (L) or transversal (T). (**) Ground motion data is only available in one horizontal direction.